Refractory Properties of Cochlear Implant-Induced Spiking in Auditory Nerve Fibers are Dependent on Location of Stimulation and Voltage-Gated Channel Type Distribution

Jason Boulet[1,2] **and Ian Bruce**[1,2,3]

Auditory Engineering Laboratory[1], McMaster Integrative Neuroscience Discovery & Study[2],
Department of Electrical & Computer Engineering[3], McMaster University, Hamilton, ON, Canada

Abstract

Background Experimental work has demonstrated that auditory nerve fibers (ANFs) of cats cannot fully respond to high rates of electrical stimulation, thus reducing the information transfer to the brain. Miller et al. (2001) have shown that a limiting factor of the reduced spike information transfer can be attributed to the neuron's refractory period. A computational model of a node of Ranvier of the ANF (Negm and Bruce, 2008) suggested that low-threshold potassium (KLT) and hyperpolarization-activated cyclic nucleotide-gated cation (HCN) channels (Yi et al., 2010) might be responsible for a larger refractory period (Negm and Bruce, in prep.).

Methods We extend that work with a simulation study taking into account ANF morphology (Woo et al., 2010) to consider the differential spiking activity as a function of 1) the location of electrical stimulation and 2) nodal channel composition at important locations along the ANF. Specifically, we test three ANF models variants: A) only fast Nav and delayed-rectifier Kv at all nodes, B) with the addition of KLT & HCN channels (Yi et al., 2010) at the first peripheral node and on the nodes of Ranvier neighboring the soma and C) by expanding the distribution of KLT channels to all nodes (Bortone et al., 2006).

Results In general, we observed the absolute refractory period of model C to be the greatest followed by model B, then by model A. Models B and C contrasted with model A by having a greater probability of spike initiation at the location of stimulation. Model A did not show a strong relative refractory period at its peripheral nodes. We argue that the washout of the relative refractory period in this region was dependent on the low correlation between the location of the stimulating electrode and the location of spike initiation.

Conclusion Preliminary results indicate that model C is most consistent with the published physiological data. In addition to the KLT & HCN channels of model C, other ion channel types may be necessary to explain all aspects of refractory behavior observed in vivo.

This research was supported by the Natural Sciences and Engineering Research Council of Canada (Discovery Grant #261736).

I. INTRODUCTION

- Recent studies have shown that electrically stimulated type I cat ANFs undergo drops in spike rate over the duration of a pulse train for high pulses rates (Zhang et al., 2007). Computational models of the ANF based on the Hodgkin–Huxley equations containing only Nav and Kv channels do not adequately describe these decrements in spike rate.
- Miller et al. (2001) has shown that the duration of refraction can vary greatly across ANFs, which is also difficult to explain with only Nav and Kv channels.
- Yi et al. (2010) have experimentally found HCN channels at the first peripheral node (or terminal) and the nodes neighboring the soma in mouse spiral ganglion cells. KLT channels have been localized on ANF axons entering rat cochlear nucleus (Bortone et al., 2006).
- A computational membrane-node model of the cat ANF incorporating Nav, Kv, KLT and HCN channels has shown that the HCN and KLT channels can produce increasing spike-rate adaptation and accommodation with increasing stimulation rate (Negm and Bruce, 2008), as well as increased refractory periods (Negm and Bruce, in prep.).
- We built a compartmental model of the cat ANF to better understand how refraction depends on the location and populations of voltage-gated ion channel species (Nav, Kv, KLT and HCN) and the location and rate of electrical stimulation from a CI.
- To simulate the activity of various ion channels types, we utilize stochastic ion channel models, because the resulting fluctuations in excitability are thought to be behaviorally significant for CI users (Bruce et al., 1999a,b).

II. METHODS: Ion Channel (In-)Activation and Time Constants

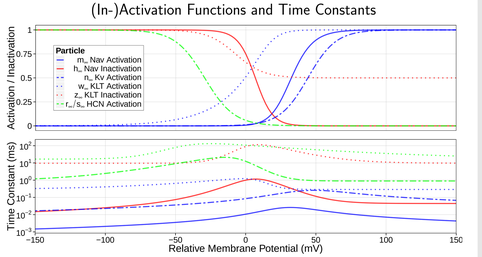

Figure 1 : Steady-state activation/inactivation functions and time constants at 37°C. We adjusted w_∞, z_∞, r_∞ and s_∞ from 22°C to 37°C (Cartee, 2000; Rothman and Manis, 2003).

II. METHODS: ANF Models

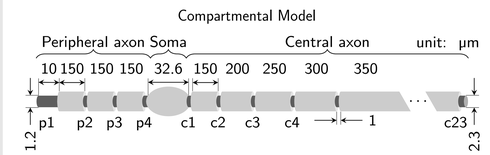

Figure 2 : Feline ANF morphology is based on Woo et al. (2010). The soma is myelinated, which contrasts with the mouse and human ANF.

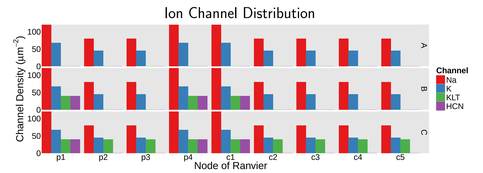

Figure 3 : Hossain et al. (2005) found high densities of Nav1.6 channels located at p1, p4 and c1 in the mouse ANF. Yi et al. (2010) have shown HCN channels at the same nodes in mouse spiral ganglion cells. KLT channels have been localized on ANF axons entering rat cochlear nucleus (Bortone et al., 2006).

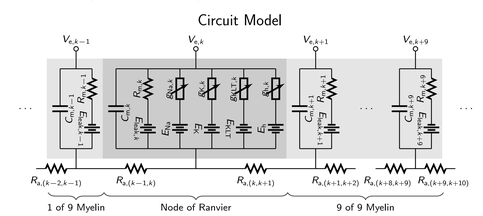

Figure 4 : The circuit model is solved as a discretized ($\Delta t = 2.5$ µs) partial differential equation (Mino et al., 2004) via time-centered Crank–Nicholson, also used in the neural simulation environment NEURON (Carnevale and Hines, 2006).

II. METHODS: Ion Channel Simulation

Channel kinetics obey continuous-time discrete-state Markov processes. The state transition diagrams for Nav, Kv (Mino et al., 2002), KLT (Negm and Bruce, 2008) and HCN1,4 (Liu and Davis, 2012) are shown in Table 1. Red states indicate fully open states that contribute to conducting ionic current. We simulated the 4 voltage-gated ion channel types with a channel number tracking algorithm (Chow and White, 1996; Mino et al., 2002).

Table 1 : State transition diagrams

Nav	Kv
$m_0h_0 \underset{\beta_m}{\overset{3\alpha_m}{\rightleftharpoons}} m_1h_0 \underset{2\beta_m}{\overset{2\alpha_m}{\rightleftharpoons}} m_2h_0 \underset{3\beta_m}{\overset{\alpha_m}{\rightleftharpoons}} m_3h_0$ $\alpha_h \downarrow\uparrow \beta_h \quad \alpha_h \downarrow\uparrow \beta_h \quad \alpha_h \downarrow\uparrow \beta_h \quad \alpha_h \downarrow\uparrow \beta_h$ $m_0h_1 \underset{\beta_m}{\overset{3\alpha_m}{\rightleftharpoons}} m_1h_1 \underset{2\beta_m}{\overset{2\alpha_m}{\rightleftharpoons}} m_2h_1 \underset{3\beta_m}{\overset{\alpha_m}{\rightleftharpoons}} m_3h_1$	$n_0 \underset{\beta_n}{\overset{4\alpha_n}{\rightleftharpoons}} n_1 \underset{2\beta_n}{\overset{3\alpha_n}{\rightleftharpoons}} n_2 \underset{3\beta_n}{\overset{2\alpha_n}{\rightleftharpoons}} n_3 \underset{4\beta_n}{\overset{\alpha_n}{\rightleftharpoons}} n_4$
KLT	**HCN**
$w_0z_0 \underset{\beta_w}{\overset{4\alpha_w}{\rightleftharpoons}} w_1z_0 \underset{2\beta_w}{\overset{3\alpha_w}{\rightleftharpoons}} w_2z_0 \underset{3\beta_w}{\overset{2\alpha_w}{\rightleftharpoons}} w_3z_0 \underset{4\beta_w}{\overset{\alpha_w}{\rightleftharpoons}} w_4z_0$ $\alpha_z \downarrow\uparrow \beta_z \quad \alpha_z \downarrow\uparrow \beta_z \quad \alpha_z \downarrow\uparrow \beta_z \quad \alpha_z \downarrow\uparrow \beta_z$ $w_0z_1 \underset{\beta_w}{\overset{4\alpha_w}{\rightleftharpoons}} w_1z_1 \underset{2\beta_w}{\overset{3\alpha_w}{\rightleftharpoons}} w_2z_1 \underset{3\beta_w}{\overset{2\alpha_w}{\rightleftharpoons}} w_3z_1 \underset{4\beta_w}{\overset{\alpha_w}{\rightleftharpoons}} w_4z_1$	$r_0 \underset{\beta_r}{\overset{2\alpha_r}{\rightleftharpoons}} r_1 \underset{2\beta_r}{\overset{\alpha_r}{\rightleftharpoons}} r_2$ $s_0 \underset{\beta_s}{\overset{\alpha_s}{\rightleftharpoons}} s_1$

II. METHODS: Electrical Stimulation

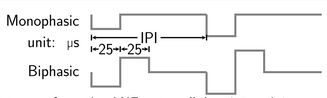

- Three distances from the ANF: intracellular, 0.5 and 1 mm
- Nine sites of stimulation, over nodes p1 to c5
- Monophasic (cathodic) and biphasic (cathodic, then anodic)
- Spherical monopolar extracellular electrode radius: 150 µm
- Inter Pulse Intervals (IPIs) ranging from 0.3 to 10 ms
- 1st pulse amplitude: $I_1 = (1 + 3\text{RS})\,\theta$, 2nd pulse: variable
- Successfully propagated spike is voltage discriminated at c17

III. RESULTS: Single-Pulse Response

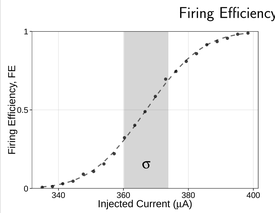

Figure 5 : FE is the probability of a spike given a single pulse of current input. Data points are the mean values from 1000 simulation trials and are fit to an integrated Gaussian (Bruce et al., 1999a). The threshold current θ is the current at FE = 0.5 and the relative spread is RS = σ/θ. This example is the response from an electrode placed 0.5 mm above node c3.

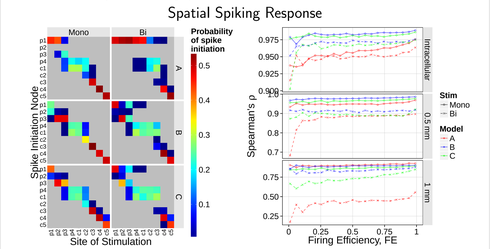

Figure 6 : **(left)** Probability of spike initiation from single pulse stimulation. Results were gathered from 1000 simulation trials. Probability is mapped onto a color as function of the stimulated site (x-axis) and the spike initiation node (y-axis). Gray values indicate no spike. This figure shows the response for an electrode 0.5 mm away from the ANF at FE = 0.5. **(right)** Spearman's correlation (ρ). This is a summary of the plot on the left, but over all FE's and distances.

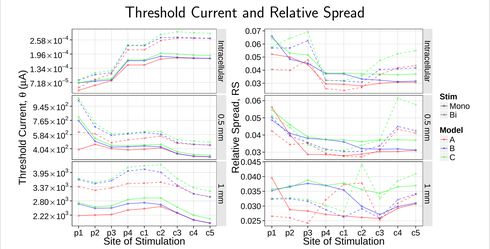

Figure 7 : **(left)** Threshold current (θ) and **(right)** Relative Spread (RS) across all nodes over 1000 trials.

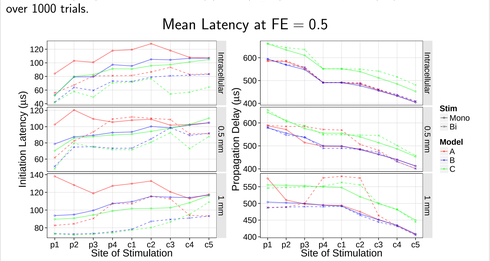

Figure 8 : Mean Latency at FE = 0.5 over 1000 trials. **(left)** Initiation latency and **(right)** propagation delay. Both components sum to give the time the spike takes to arrive at node c17.

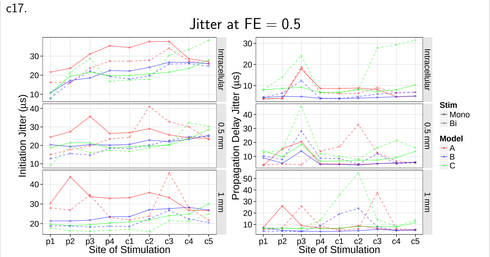

Figure 9 : Jitter at FE = 0.5 for 1000 trials. **(left)** Initiation latency and **(right)** propagation delay jitter.

III. RESULTS: Spike Initiation and Propagation

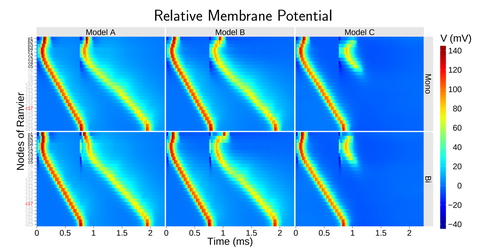

Figure 10 : One example of a simulation of the relative membrane potential as a function of time and node of Ranvier along the ANF. For these particular trials, we present the ANF with a stimulus 0.5 mm over node p4, with an IPI of 750 µs and a second-pulse magnitude of 1.5θ.

III. RESULTS: Threshold Ratio (2nd-pulse/1st-pulse)

We fit the threshold data to

$$\theta_{2/1} = \frac{a_1 + a_2}{a_1\left(1 - \exp\left[-\left(\frac{\text{IPI}-\tau_{\text{abs}}}{\tau_1}\right)\right]\right) + a_2\left(1 - \exp\left[-\left(\frac{\text{IPI}-\tau_{\text{abs}}}{\tau_2}\right)\right]\right)} \quad (1)$$

which has been found to fit the threshold ratio data better with two time scales (Negm and Bruce, in prep.) than with one (Miller et al., 2001).

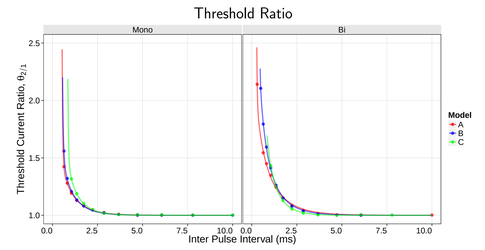

Figure 11 : Second-to-first pulse threshold ratio ($\theta_{2/1}$). Second pulse thresholds are derived from 100 simulation trials fit to an integrated Gaussian function. In these cases above, we used a stimulus 0.5 mm over node c3.

III. RESULTS: Time Scales of Refraction

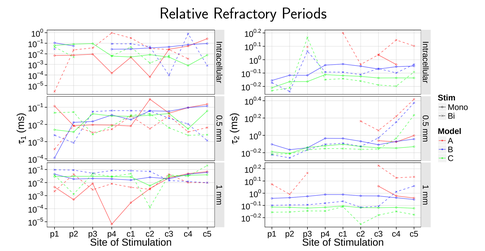

Figure 12 : Relative refractory periods **(left)** τ_1 and **(right)** τ_2.

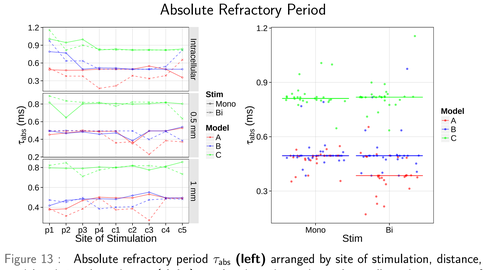

Figure 13 : Absolute refractory period τ_{abs} **(left)** arranged by site of stimulation, distance, model and stimulus, whereas **(right)** we also show the median values collapsed across site of stimulation and distance.

III. RESULTS: Spike-Rate Adaptation

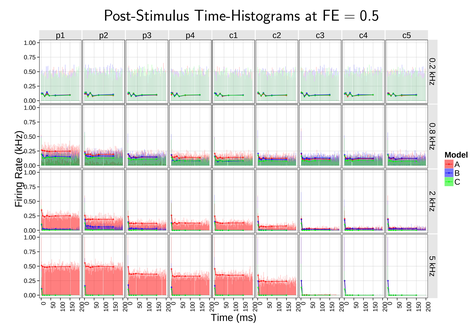

Figure 14 : PSTHs for our model ANFs. The responses are shown for stimulated nodes p1 to c5 at the stimulus rates 200, 800, 2000 and 5000 kHz with monophasic stimulation and at a distance of 0.5 mm. The PSTHs were generated by averaging across 100 simulation trials of 200 ms for two sets of time-bins (Zhang et al., 2007).

IV. CONCLUSIONS

- Single-pulse threshold currents in models C>B>A.
- Models B and C show a stronger relationship between where the stimulus is delivered and where the spike is initiated than model A
- Models B and C show the best fits to the two-time scale refractory function, as evidenced by the unwieldy relative refractory time constants of model A.
- Model C has a significantly larger absolute refractory period than models A and B. Therefore, cell-wide distribution of KLT channels plays a major role in increasing the absolute refractory period.
- Model A displays evidence of summation for high stimulus rates of 2000 and 5000 pulses/s, similarly to Heffer et al. (2010) in guinea pig ANF.
- Further computational studies must be done to address the relative impacts of refraction, spike-rate adaptation, accommodation and facilitation (summation) on changes in spike rate over the duration of a pulse train for high stimulation rates.

References

Bortone, D. S., Mitchell, K., and Manis, P. B. (2006). Developmental time course of potassium channel expression in the rat cochlear nucleus. *Hearing Research*, 211(1-2):114–125.

Bruce, I. C., White, M. W., Irlicht, L. S., O'Leary, S. J., and Clark, G. M. (1999a). The effects of stochastic neural activity in a model predicting intensity perception with cochlear implants: low-rate stimulation. *IEEE Transactions on Biomedical Engineering*, 46(12):1393–1404.

Bruce, I. C., White, M. W., Irlicht, L. S., O'Leary, S. J., Dynes, S., Javel, E., and Clark, G. M. (1999b). A stochastic model of the electrically stimulated auditory nerve: single-pulse response. *IEEE Transactions on Biomedical Engineering*, 46(6):617–629.

Carnevale, N. T. and Hines, M. L. (2006). *The NEURON Book*. Cambridge University Press.

Cartee, L. A. (2000). Evaluation of a model of the cochlear neural membrane. II: comparison of model and physiological measures of membrane properties measured in response to intrameatal electrical stimulation. *Hearing Research*, 146(1-2):153–166.

Chow, C. and White, J. A. (1996). Spontaneous action potentials due to channel fluctuations. *Biophysical Journal*, 71:3013–3021.

Heffer, L. F., Sly, D. J., Fallon, J. B., White, M. W., Shepherd, R. K., and O'Leary, S. J. (2010). Examining the auditory nerve fiber response to high rate cochlear implant stimulation: chronic sensorineural hearing loss and facilitation. *Journal of Neurophysiology*, 104(6):3124–3135.

Hossain, W. A., Antic, S. D., Yang, Y., Rasband, M. N., and Morest, D. K. (2005). Where is the spike generator of the cochlear nerve? Voltage-gated sodium channels in the mouse cochlea. *Journal of Neuroscience*, 25(29):6857–6868.

Liu, Q Manis, P. and Davis, R. (2012). Heterogeneous Distribution of I_h and HCN Channels in Murine Spiral Ganglion Neurons. *MidWinter Meeting: Association for Research in Otolaryngology*.

Miller, C. A., Abbas, P. J., and Robinson, B. (2001). Response properties of the refractory auditory nerve fiber. *Journal of the Association for Research in Otolaryngology*, 2(3):216–232.

Mino, H., Rubinstein, J. T., Miller, C. A., and Abbas, P. J. (2004). Effects of Electrode-to-Fiber Distance on Temporal Neural Response With Electrical Stimulation. *IEEE Transactions on Biomedical Engineering*, 51(1):13–20.

Mino, H., Rubinstein, J. T., and White, J. A. (2002). Comparison of algorithms for the simulation of action potentials with stochastic sodium channels. *Annals of Biomedical Engineering*, 30(4):578–587.

Negm, M. H. and Bruce, I. C. (2008). Effects of I_h and I_{KLT} on the response of the auditory nerve to electrical stimulation in a stochastic Hodgkin-Huxley model. *Conference proceedings: Annual International Conference of the IEEE Engineering in Medicine and Biology Society IEEE Engineering in Medicine and Biology Society Conference*, 2008:5539–5542.

Rothman, J. S. and Manis, P. B. (2003). The Roles Potassium Currents Play in Regulating the Electrical Activity of Ventral Cochlear Nucleus Neurons. *Journal of Neurophysiology*, 89(6):3097–3113.

Woo, J., Miller, C. A., and Abbas, P. J. (2010). The dependence of auditory nerve rate adaptation on electric stimulus parameters, electrode position, and fiber diameter: a computer model study. *Journal of the Association for Research in Otolaryngology*, 11(2):283–296.

Yi, E., Roux, I., and Glowatzki, E. (2010). Dendritic HCN Channels Shape Excitatory Postsynaptic Potentials at the Inner Hair Cell Afferent Synapse in the Mammalian Cochlea. *Journal of Neurophysiology*, 103(5):2532–2543.

Zhang, F., Miller, C. A., Robinson, B. K., Abbas, P. J., and Hu, N. (2007). Changes across time in spike rate and spike amplitude of auditory nerve fibers stimulated by electric pulse trains. *Journal of the Association for Research in Otolaryngology*, 8(3):356–372.

bouletjw@mcmaster.ca